ACCEPTED BY APJ 2005 MARCH 10
Preprint typeset using LaTeX style emulateapj v. 6/22/04

arXiv:astro-ph/0503376v1 17 Mar 2005

THE DEEP GROTH STRIP SURVEY. I. THE SAMPLE[1,2]

NICOLE P. VOGT[3]
New Mexico State University, Department of Astronomy,
P.O. Box 30001, Dept 4500, Las Cruces, NM 88003

AND

DAVID C. KOO, ANDREW C. PHILLIPS, KATHERINE WU[4], S. M. FABER, CHRISTOPHER N. A. WILLMER[5], LUC SIMARD[6], BENJAMIN J. WEINER, GARTH D. ILLINGWORTH, KARL GEBHARDT[7], CARYL GRONWALL[8], RAFAEL GUZMÁN[9], MYUNGSHIN IM[10], & VICKI SARAJEDINI[9]
University of California Observatories / Lick Observatory, Department of Astronomy and Astrophysics, University of California, Santa Cruz, CA 95064

AND

EDWARD J. GROTH[11], JASON RHODES[12], ROBERT BRUNNER[13], ANDREW CONNOLLY[14], ALEX SZALAY[15], RICHARD KRON[16], & ROGER BLANDFORD[17]

Accepted by ApJ 2005 March 10

ABSTRACT

The Deep Extragalactic Exploratory Probe (DEEP) is a multi-phase research program dedicated to the study of the formation and evolution of galaxies and of large scale structure in the distant Universe. This paper describes the first five-year phase, denoted DEEP1. A series of ten DEEP1 papers will discuss a range of scientific topics (*e.g.*, the study of photometric and spectral properties of a general distant galaxy survey, the evolution observed in galaxy populations of varied morphologies). The observational basis for these studies is the Groth Survey Strip field, a 127 square arcminute region which has been observed with the Hubble Space Telescope in both broad I-band and V-band optical filters and with the Low Resolution Imaging Spectrograph on the Keck Telescopes. Catalogs of photometric and structural parameters have been constructed for 11,547 galaxies and stars at magnitudes brighter than 29, and spectroscopy has been conducted for a magnitude-color weighted subsample of 818 objects. We evaluate three independent techniques for constructing an imaging catalog for the field from the HST data, and discuss the depth and sampling of the resultant catalogs. The selection of the spectroscopic subsample is discussed, and we describe the multifaceted approach taken to prioritizing objects of interest for a variety of scientific subprograms. A series of Monte Carlo simulations then demonstrates that the spectroscopic subsample can be adequately modeled as a simple function of magnitude and color cuts in the imaging catalog.

Subject headings: cosmology: observations — galaxies: formation — galaxies: distances and redshifts — galaxies: evolution — galaxies: structure

1. INTRODUCTION

The advent of 8-meter class ground–based optical and infrared telescopes, the latest generation of radio and submillimeter arrays, and the high spatial resolution of the Hubble Space Telescope (HST) have produced a 100-fold increase in observational resources with which to study the evolution of galaxies in the local and in the distant Universe.

The commissioning of the wide–field multifiber systems used by the 2dF Galaxy Redshift Survey (Colless et al. 2001) and the Sloan Digital Sky Survey (Abazajian et al. 2003) have finally enabled the construction of large samples of local galaxies, for which a wealth of detailed structural parameters have been determined. Parallel efforts with large optical telescopes, leveraged by the 100-fold advantage of the latest generation of multi-object spectrographs, are beginning to generate samples of comparable impact in the distant galaxy field. These will allow statistically significant analyses of the evolution of varied populations of galaxies from the present to redshifts $z \sim 1$ (extending over half of the age of the Universe).

The Deep Extragalactic Exploratory Probe (DEEP) is a multi-phase program focused on the study of the formation and evolution of galaxies and of large scale structure across this redshift range. The second phase (DEEP2), underway at present, uses a sample of $\sim 50,000$ galaxies with ground–based multi-band photometry and spectroscopic redshifts obtained with the recently commissioned Deep-Imaging Mul-

Electronic address: nicole@nmsu.edu

[1] Based on observations obtained at the W. M. Keck Observatory, which is operated jointly by the California Institute of Technology and the University of California.

[2] Based in part on observations with the NASA/ESA *Hubble Space Telescope*, obtained at the Space Telescope Science Institute, which is operated by AURA, Inc., under NASA contract NAS 5–26555.

[3] University of California, Santa Cruz, CA 95064
[4] University of Tampa, Tampa, FL 33606
[5] On leave from Observatório Nacional, Rio de Janeiro, Brazil
[6] National Research Council of Canada, Herzberg Institute of Astrophysics, Victoria V9E 2E7, Canada
[7] University of Texas, Austin, TX 78723
[8] Pennsylvania State University, University Park, PA 16802
[9] University of Florida, Gainesville, FL 32611
[10] Seoul National University, Seoul, South Korea
[11] Princeton University, Princeton, NJ 08544
[12] Jet Propulsion Laboratory, Pasadena, CA 91109
[13] University of Illinois, Urbana, IL 61801
[14] University of Pittsburgh, Pittsburgh, PA 15260
[15] John Hopkins University, Baltimore, MD 21218
[16] Fermi National Accelerator Laboratory, Batavia, IL 60510
[17] Stanford University, Stanford, CA 94305

tiobject Spectrograph (DEIMOS) on the Keck 2 Telescope. This paper describes the first five- year pilot phase (DEEP1). The primary observational basis is the Groth Survey Strip (GSS) field, a 127 square arcminute region which has been observed with HST in both broad I-band and V-band optical filters and with the Low Resolution Imaging Spectrograph (LRIS) on the Keck Telescopes.

There have been a number of ambitious surveys bridging the gap between the local and the distant Universe, and increasing the number counts of faint galaxies over the last ten years (for an overview of previous work see Koo & Kron 1992 and Ellis 1997). Among these works we can cite *cf.*, the ESS survey, Arnouts et al. 1997, the LDSS survey, Colless et al. 1999; the CNOC and CNOC2 surveys, Yee et al. 1996, Yee et al. 2000; the Hawaii Deep Fields Survey, Cowie, Songalia, Hu, & Cohen 1996.

Three surveys of comparable size and depth to the DEEP1 GSS survey are the Canada-France Redshift Survey (CFRS, Lilly et al. 1995), the Caltech Faint Galaxy Redshift Survey (CFGRS, Cohen et al. 2000), and the Very Large Telescope Deep Survey with the VIMOS spectrograph (VLT+VIMOS, Le Fèvre et al. 2004). Figure 1 places the DEEP1 survey in the context similar optical redshift surveys of the distant galaxy population, with a direct comparison to the CFRS and CFGRS data sets. The pioneering CFRS is a ~ 600 galaxy (250 of which have HST imaging) magnitude-limited survey which extends to $I_{AB} = 22.5$ with a median redshift of $z = 0.56$ (Crampton et al. 1995). It is 1.5 magnitudes shallower than the nominal limit of DEEP1, even though the median redshifts are similar (*i.e.*, the DEEP1 survey focuses on intrinsically fainter galaxies), due to differences in the survey sampling algorithms and to common difficulties in obtaining redshifts for galaxies beyond $z \sim 1.1$. The CFGRS survey is focused upon the northern Hubble Deep Field (HDF-N), with a comparable number of redshifts ($z_{med} = 0.7$) for galaxies extending to $R = 24$ in the HDF-N proper and to $R = 23$ in the Flanking Fields (Cohen et al. 2000). The recent VLT+VIMOS survey centers upon the southern GOODS field (Giavalisco et al. 2004), containing 784 redshifts for galaxies with HST imaging and an additional 815 in the surrounding areas. The spectral program extends down to $I_{AB} = 24$, as does the DEEP1 survey, with a median redshift of 0.73.

Three features distinguish the DEEP GSS survey in this context. First, the field is a continuous band extending over 40×3 arcminutes on the sky (covering a range of 38 comoving Mpc by redshift $z = 1$). Second, the complete HST imaging in both V-band and I-band allows for the measurement of a uniform set of rest-frame colors and structural parameters out to redshifts $z \sim 1$. Third, the spectral resolution of 3–4 Å (versus 10 Å for the CFGRS and 40 Å for the CFRS) enables both resolution of the [O II] λ3727 doublet feature (2.7 Å rest-frame split) and that detailed internal kinematic measurements be made for individual objects.

2. OVERVIEW

We have already published several papers which draw upon the DEEP1 GSS data set. Initial results of the general redshift survey were discussed in Koo et al. (1996), while Vogt et al. (1996, 1997) found modest amounts of evolution for disk galaxies in the field, Simard et al. (1999) explored the effect of surface brightness levels in object detection from the HST images, and Im et al. (2001) studied the kinematics of massive blue spheroidal galaxies. This paper is the first in a formal series dedicated to these DEEP program data. We

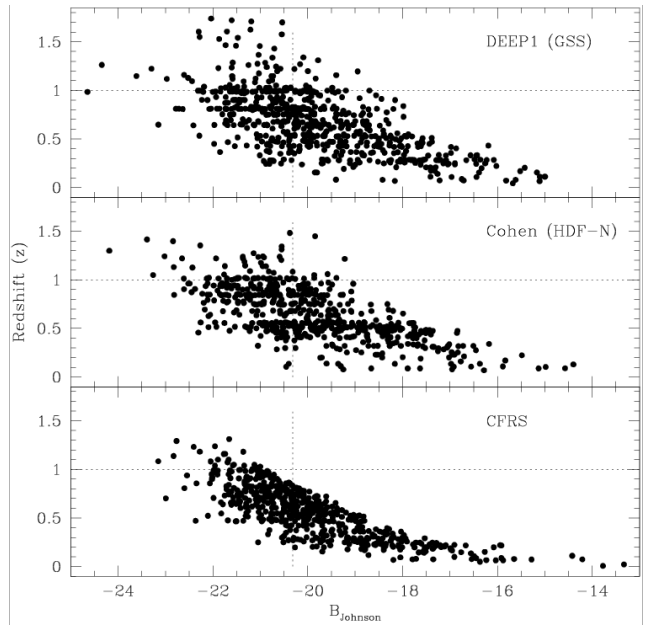

FIG. 1.— The distribution of redshift z versus absolute magnitude, for (a) DEEP1 (Weiner et al. 2005a), (b) the Caltech Faint Galaxy Redshift Survey (Cohen et al. 2000), and (c) the CFRS survey (Lilly et al. 1995; Le Fèvre et al. 1995; Hammer et al. 1995). The dotted vertical line shows the location of $M^{\star}$, and dotted horizontal lines mark $z = 1$ for each survey. We note that the lack of galaxies at redshifts well beyond $z = 1$ in DEEP1 is an artifact of limited spectral coverage in the extreme red, rather than being caused by a dramatic change in the underlying distribution, while the enhanced counts at $z = 1$ are due to large scale structure across the field (*cf.*, Le Fèvre et al. 1994, Koo et al. 1996). The DEEP1 survey goes ~ 1.5 magnitude deeper than the CFRS, comparable to the depth of Cohen et al., and is distinguished by complete HST+WFPC2 coverage.

outline below the immediate papers published and planned within the DEEP Groth Strip Survey Sequence:

- I The Sample (this paper)
- II HST Structural Parameters of Galaxies in the Groth Strip (Simard et al. 2002)
- III Redshift Catalog and Properties of Galaxies (Weiner et al. 2005a)
- IV Formation and Evolution of Disk Galaxies from a Sample of Spatially Extended Velocity Curves (N. P. Vogt et al. 2005, in preparation)
- V Evolution of Field Galaxies in Luminosity and Velocity Widths (B. J. Weiner et al. 2005b, in preparation)
- VI Evolution of faint AGN (V. L. Sarajedini et al. 2005, in preparation)
- VII The Metallicity of Field Galaxies at $0.26 < z < 0.82$ and the Evolution of the Luminosity-Metallicity Relation (Kobulnicky et al. 2003)
- VIII Evolution of Luminous Bulges at High Redshift (Koo et al. 2005)
- IX Evolution of the Fundamental Plane of Field Galaxies (Gebhardt et al. 2003)
- X Number Density and Luminosity Function of Field E/S0 Galaxies at $z < 1$ (Im et al. 2002)

Updates to the our mission statement can be found on the DEEP website (`http://deep.ucolick.org`), as well as a complete data release of the GSS data.

All Johnson-Cousins magnitudes used in this paper are on the Vega system (with the exception of those shown in Figure 5, which uses the AB system); transformations between

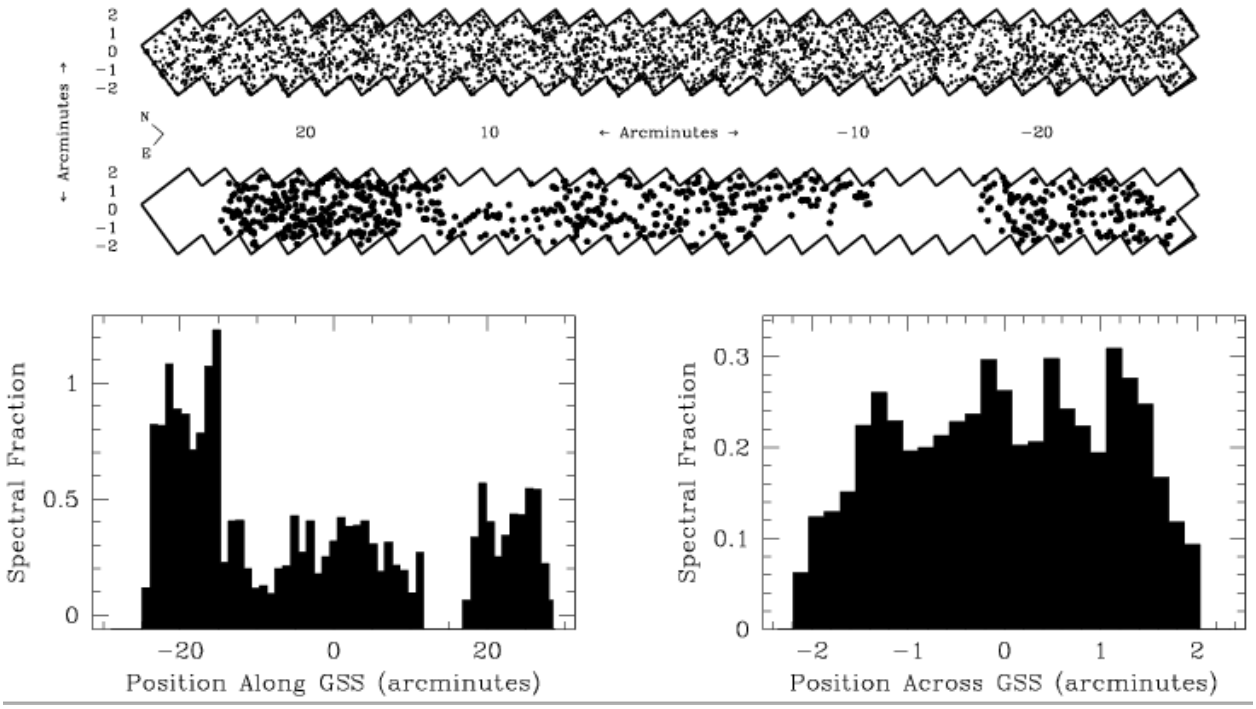

FIG. 2.— The distribution of objects along the GSS. The top two panels show the extent of the strip on the sky, running from the first chevron (number 4, at the northeastern extreme) to the 28th chevron (number 31) and covering an area roughly forty by three arcminutes. The upper panel shows the distribution of all objects detected in either or both I_{814} and V_{606} passbands in the FOCAS catalog, and the lower panel the subset for which we have obtained Keck+LRIS spectra. The lower panels show the fraction of targets within the FOCAS catalog down to the magnitude limit of our general redshift survey for which we have spectra, as a function of position along (left panel) and across (right panel) the GSS.

the Vega and AB systems are listed in Appendix B. We have chosen to use a ΛCDM cosmogony with $h = 0.7, \Omega_M = 0.3$, and $\Omega_\Lambda = 0.7$ for this entire series of papers, unless otherwise noted.

3. FIELD HISTORY

The GSS field is a high latitude field in the HST continuous viewing zone with no bright stars and with marginal levels of galactic extinction. The primary science drivers for the initial HST+WFPC2 Cycle 4 observations were to study cosmology and galaxy evolution by evaluating the evolution of number counts, the luminosity function, colors and morphology, and the distribution of galaxies and of clusters in redshift.

The field is defined as the spatial position of a long band of imaging data from two Hubble Space Telescope and Wide Field Planetary Camera (HST+WFPC2) programs (GTO 5090 with PI E. Groth; GTO 5109 with PI J. Westphal). They consist of 28 overlapping WFPC2 chevrons, numbered 4 through 31 because three chevrons originally placed at the northeast end of the strip were discovered to lie too far from appropriate guide stars and were replaced with three new pointings at the south-west end. The field is oriented at 45° eastwards of north, centered at (14^h17^m, +52°), as shown in Figure 2, has a total area of 127 square arcminutes, and lies at a Galactic latitude of $b \sim 60°$.

Though the strip of WFPC2 chevrons runs along an angle of 45° eastwards of north, the orientation of the roll angle, equivalent to the axis of symmetry of each chevron along the line bisecting each chip 3 from pixel (0,0) to (800,800), lies at 40.5° eastwards of north. Because of the 4.5° offset, chips 2 of each chevron overlap slightly within a region of size 79″ by 21″ with the chips 3 of the next chevron along the strip. These overlap regions were used to align the chevrons together in to a single supermosaic for the data taken within each passband, as were diffraction spikes that crossed chip to chip boundaries.

Each chevron has been imaged for 2,800 seconds in a broad V filter (F606W, V_{606}) and for 4,400 seconds in a broad I filter (F814W, I_{814}), with the exception of the single deep chevron (number 7, fourth from the northeast edge, centered at $14^h17^m30^s$, $+52°30^m$) which was observed for 24,400 seconds in V_{606} and for 25,200 seconds in I_{814}. Images for the primary program were constructed by rejecting cosmic rays from four undithered exposures in each filter, each lasting 700 seconds in V or 1100 seconds in I. (A series of four orbits were spent observing each chevron, with each orbit consisting of a single exposure in V and a single exposure in I.) For the deeply imaged chevron, eight 2100 second and four 1900 second exposures, each taking a full orbit, were combined in V, and twelve 2100 second exposures were combined in I.

Additional WFPC2 optical imaging data have been collected along the GSS by a variety of authors and teams, including $3 \times 2,800$ seconds in a broad B filter (F450W, B_{450}) and $3 \times 2,800$ seconds in I_{814} (GO 5449 with PI S. Lilly) for a chevron which overlaps by 70% with the third GSS chevron (number 6). In Cycle 9, all GSS chevrons but the deeply imaged number 7 were re-imaged for 700 seconds with V_{606} (GO 8698 with PI J. Mould). A small number of objects within the Groth Strip have been selected for additional observations with other HST instruments (NICMOS GO 7871 with PI A. Connolly; NICMOS GO 7883, STIS GO 10249 with PI N. Vogt).

Keck+LRIS ground-based BRI imaging of the northeast

one-third portion of the Groth Strip has also been conducted by the DEEP team. Shallower UBRI imaging (down to U = 25, B = 25.5, R = 23.4, I = 23.8 for S/N = 10) of the same region was done at KPNO, and may be extended as a part of the DEEP2 survey. Additional data have been obtained at longer wavelengths for parts of the field using SCUBA and the VLA (Fomalont et al. 1991), as well fairly extensive data in K-band (*cf.*, Cristóbal-Hornillos et al. 2003; Conselice et al. 2005). The field also has been or will be observed as a part of numerous large survey programs (*e.g.*, the CFHT Legacy Survey; also with XMM, Chandra, Galex, JWST, and ISO). This list is not a complete census; we simply wish to illustrate that a significant amount of observational resources, spanning multiple wavelength regimes, have been devoted to this portion of the sky.

4. ASTROMETRIC SOLUTION

An initial astrometric and photometric analysis of the GSS WFPC2 data was completed with the Faint Object Classification and Analysis System (FOCAS; Jarvis & Tyson, 1981) for 11,547 objects down to 33rd magnitude in $(V_{606}+I_{814})/2$.

An independent astrometric solution was created for a supermosaic in each passband composed of all 28 chevrons, by first transforming the individual chip coordinates to a common coordinate system based on the polynomial coordinates derived by Holtzman et al. 1994. The rms residual errors in x and in y on each chip are equal or less than $0.02''$ along the entire strip, as determined by evaluation of the objects observed on two chevrons in the overlap regions. The values are fairly uniform, though we note that the residuals on the chip 3 regions are slightly higher on average (by 25%) than those for chips 2 and 4.

There are six HST guide star catalog objects within the strip, which were used for astrometric zero pointing. The error in guide star coordinates is a sizable fraction of an arcsecond (we estimate $0.5''$ in each coordinate), which will affect the absolute calibration. Star positions were measured on the WFPC2 chevrons by measuring the intersections of diffraction spikes; in one case the stellar flux peak could also be measured, and the two techniques agreed to within a pixel. An rms residual of $0.33''$ was obtained by using all six stars, and the best, final fit was obtained from four stars (rms value of $0.11''$), by discarding two stars which fell very close to the edge of the WFPC2 chips.

Because of their late attachment to the Cycle 4 observational program, we note that chevrons 28 - 31 were taken with an offset in roll angle of 0.6004° relative to the remainder of the strip (the roll angle was specified to only 0.01° in the original observing proposal). In contrast, the average error in the roll angle was measured to be 0.2° across the entire Cycle 4 WFPC2 data set. These factors were taken into account in the astrometric solutions. A comparison of the final solutions for the V_{606} and I_{814} data yielded errors of less than $0.01''$ between the two passbands; this close agreement allowed us to overlay the two mosaics on top of each other to produce a valid color map of the entire strip.

Summarizing the primary sources of error in the astrometric model, small scale (*i.e.*, chevron scale) errors are controlled by the chip distortion model ($0.02''$ rms), chevron offset determination ($0.025''$ rms), and roll errors ($0.025''$ rms in the chip corners furthest from the chevron center), leading to a total rms error of $0.035''$. This translates into rms errors of order $0.1''$ in right ascension and declination, and a rotational uncertainty of 0.017°, along the entire strip. When evaluating individual objects, one must of course also take into account the errors in object centroiding (discussed below).

5. PHOTOMETRIC CATALOGS

The photometric catalog was created using FOCAS within the Image Reduction and Analysis [18] (IRAF) environment to determine valid detections, classified as 10,955 galaxies, 436 stars, and 156 objects of uncertain morphology (*e.g.*, fuzzy, diffuse) where classification was done by rescaling (broadening and narrowing) the point spread function (PSF) to create a set of templates then used to best match each object's flux distribution. The objects identified as stars span the full range of magnitude of the sample, and represent a conservative estimate of the stellar contribution. The spectral subsample contains 37 objects classified as stars; divided between 28 objects at $z = 0$ and nine for which a redshift could not be determined (due to *e.g.*, faint flux, lack of distinguishing features). An additional 128 spectra were obtained for stars which had been misidentified as galaxies by FOCAS. In summary, FOCAS successfully identified from 55 to 73% of all stars brighter than 19th magnitude, dropping to the range of 10 to 22% for all magnitudes, within the spectroscopic subsample. There was in general great difficulty in distinguishing between intermediate redshift ($z \sim 0.7$) compact galaxies and stars, *e.g.*, halo M dwarfs, solely from photometric data. Note that the FOCAS object classification codes were not used during the process of selecting spectroscopic subsamples.

FOCAS operates by detecting objects of a set minimum size that register above a set threshold level above a sky background level. Background levels were determined for each chip (2 through 4, note that we did not use the planetary camera chip data, so as to maintain a uniform resolution and sensitivity throughout) and on each chevron, by examining blank rectangles of sky. The detection threshold was set to 3σ above sky background for the bulk of the GSS, and to 4.5σ for the deeply imaged field (chevron 7). When making this evaluation, the minimum object size was set to two pixels ($0.2''$) across the entire strip.

Three objects were manually added to the catalog of FOCAS detections, each being a target that fell well within the extended flux of a brighter galaxy or stellar diffraction spike and thus was not recognized as a separate object, but for which we wished to obtain a redshift nonetheless.

After each object detection, FOCAS computes an individual sky background surrounding each object. Each object was then "grown" by adding concentric rings of pixels until its total area had doubled. The grown object was then evaluated to determine its magnitude and centroid. FOCAS attempts to split blended objects automatically, but the algorithm used for this purpose was not found to be optimized for faint object detections on these images (*i.e.*, down to $(V_{606}+I_{814})/2 = 25$ completeness limit, as discussed below). It was thus necessary to examine each object by eye, to verify and on occasion to correct the division of parent objects in order to produce the proper splitting into de-blended objects. The low detection threshold and small object size also introduced spurious "noise" objects, which were filtered out by matching V_{606} and I_{814} frame detections.

One potential drawback to this technique is that the size of the detection area for a given object can vary between V_{606} and

[18] IRAF is distributed by the National Optical Astronomy Observatories, which are operated by the Association of Universities for Research in Astronomy (AURA) under cooperative agreement with the National Science Foundation.

TABLE 1
CATALOG OF APERTURE PHOTOMETRY

Identification Codes				Coordinates (J2000)		Magnitudes[d]							Selection
GSS	G[a]	B[b]	CFRS[c]	R.A.	Dec.	V_c	I_c	$V_c - I_c$	V_f	I_f	V_g	I_g	Criteria
072_4040	G82a	B08839		14:17:37.836	+52:28:58.45	22.15	20.92	1.27	20.64	19.63	19.58	20.61	disk
073_0542	G1307	B09464		14:17:46.405	+52:28:39.65	24.70	23.63	1.08	24.59	23.55	22.06	23.43	zsurvey
073_1810	G1318	B09321		14:17:42.635	+52:28:45.32	23.48	22.01	1.43	21.96	20.54	21.30	22.85	morph
073_2356	G1355	B09831		14:17:47.401	+52:29:00.50	23.51	22.89	0.64	23.42	22.82	22.55	23.09	serendip
073_3539	G1367	B09751	C14.1043	14:17:45.385	+52:29:08.27	22.04	20.35	1.77	21.19	19.65	19.60	21.12	phz

[a]See Rhodes, Refregier, & Groth (2000); [b]see Brunner, Connolly, & Szalay (1999); [c]see Lilly et al. (1995); [d]HST F606W and F814W magnitudes, V_{606} and I_{814} within 1.″5 diameter, $V_{606} - I_{814}$ within 1″ diameter; V_{606} and I_{814} measured with FOCAS; V_{606} and I_{814} measured with GIM2D.

I_{814} frames, as the data for the two bandpasses have different levels of sensitivity. In addition, an actual variation in object size can be a function of $V_{606} - I_{814}$ color, one of the key catalog parameters which was used in selecting a subsample for follow-up spectroscopic observations. Object centroiding was also done independently in each bandpass, leading to shifts in object position between the two bandpasses. Taken together, these factors might strongly affect the applicability of the "total" magnitudes derived from FOCAS for our fainter candidates.

We note that the V_{606} catalog data appear to extend more deeply than those of the I_{814} observations (*i.e.*, more objects are detected in V_{606} but not in I_{814} than the reverse). This effect becomes significant for objects fainter than 25 in V_{606}, beyond the limits of the spectral sample. Down to 25 in V_{606} and to 24 in I_{814} (*i.e.*, extrapolating a median $V_{606} - I_{814}$ color of one for non-detections), there are 171 objects detected only in V_{606} and 157 more detected only in I_{814} (and within the spectral sample only 16 targets were undetected in I_{814} and 23 were undetected in V_{606}). In contrast, when we extend these limits by one magnitude we find 1681 objects detected only in V_{606} versus 335 detected only in I_{814}, and the numbers increase to 5198 versus 760 when the entire optical catalog is evaluated.

This increase in faint V_{606} detections is caused by several factors. First, object detection was set to penetrate well into the noise, and the faint detection threshold was set independently in each bandpass and extends to fainter levels in V_{606}. Second, the narrower V_{606} point spread function (*cf.*, Casertano et al. 2000) allowed "blobby" objects to be split into multiple components, while the same group of objects (or, alternatively, the same galaxy plus H II regions) was treated as a single object with the summed, brighter magnitude in the I_{814} data.

We defined a set of object names according to the following convention. Every object within the imaging catalog received a seven-digit name, optionally ended with a single letter. The first three digits are the WFPC2 chevron number along the strip (two digits between 4 and 31, with a leading zero if necessary) and chip (single digit, one of chips 2 through 4); they are followed by an underscore symbol. The final four digits are the x and y position of the object on its chip as detected in I_{814}, if so detected (else in V_{606}), rounded off to the nearest ten pixels. For example, an object found in field 7 (the deeply imaged field) on chip 4 at coordinates (235, 516) would thus be named 074_2452.

One can conceivably (though rarely) have multiple objects with the same name (when objects are found within the same 1" square on a chip), so we also track the FOCAS-generated identification number (running from 1 to 11,543) to avoid any confusion. When we do include two such objects in the spectral sample, the second to be observed has an "a" attached to the end of its seven-digit name.

We elected to conduct a second photometric analysis of the data based on aperture magnitudes, measured with the IRAF package APPHOT. Object centroids as determined from the FOCAS I_{814} data were used to define the location of all targets within both bandpasses, supplemented by the V_{606} object centroids for those undetected in I_{814}. Aperture magnitudes were determined for both 1.0″ and 1.5″ diameter regions for each object detected by FOCAS.

We analyzed 421 objects brighter than 25th magnitude within the overlap regions of successive chips 2 and 3 twice (*i.e.*, once per separately observed chip, or chevron) to determine rms error rates. Object centroids had been fit to the chip 3 data with the FOCAS catalog; these were used to determine object positions on the overlapping chip 2 regions. The offset between successive chevrons varied by $\pm 2''$ across the entire GSS, and was determined for each chevron by examining the most compact objects in the overlap region. No rotation correction was applied, as the linear offsets were deemed sufficient. The individual derived chip 2 object positions were then allowed to shift to match the local maximum, resulting in sub-pixel corrections. Background levels were estimated on a chip-by-chip basis, and then aperture photometry was performed using set 1.0″ and 1.5″ diameter apertures for both sets of images.

The differences in flux levels were found to be fairly constant, at 0.025 ± 0.030 magnitudes throughout the I_{814} data set. Comparison values for the 1.0″ and 1.5″ apertures differed by 0.003 magnitudes, and there was no significant trend with magnitude for objects brighter than 25th magnitude. This is likely a combination of two competing effects. The brighter objects exhibit high flux levels but extend spatially beyond the aperture limits, and so small variations in centroiding between chips 2 and 3 can cause variations in estimating the aperture flux. The fainter objects are contained almost entirely within the apertures, and thus centroiding issues become less relevant, but the overall signal to noise levels decrease. The V_{606} data showed slightly larger differences between chip 2 and chip 3 measurements, at 0.035 ± 0.035 magnitudes, due in part to slightly elevated background levels.

For spectroscopic target selection, we elected to use the V_{606}

and I_{814} magnitudes as measured in the 1.5″ diameter apertures, combined with the 1.0″ diameter aperture $V_{606}-I_{814}$ colors ("Core" colors) to define object magnitudes and colors. This improved the accuracy of color measurements (*i.e.*, a relative flux measurement), particularly for faint detections, and permitted us to extend color and two-bandpass measurements to faint objects that had been detected by FOCAS in only one of the two HST bandpasses. We label this catalog of magnitudes and colors the "Core" catalog, as the object fluxes are sampled only in the core regions (*i.e.*, aperture size is constant, and does not vary with object angular size).

Table 1 shows a representative set of entries to the object catalog, available in its entirety on the DEEP web site at `http://deep.ucolick.org`. Each object is identified with its DEEP1 seven to eight element name, followed by the FOCAS catalog identification and the names (as available) in the ground-based UBRI (Brunner, Connolly, & Szalay 1999) and in the CFRS survey object catalogs. Coordinates are listed (J2000), followed by aperture V_{606} and I_{814} aperture magnitudes and $V_{606}-I_{814}$ colors. The final column indicates the selection criteria by which the object was placed on a Keck+LRIS mask, if this occurred (see discussion of keywords below).

A third photometric analysis was conducted with the galaxy modeling package GIM2D after the majority of the spectral program had been completed, to derive a detailed, extended set of structural and morphological parameters for all objects. Discussion of this "GIM2D" catalog, and its optimization, is the primary topic of Paper II (Simard et al. 2002). These data, including magnitudes as well as structural parameters, are used throughout most of the DEEP1 science papers.

Figures 3 and 4 demonstrate the relation between photometric measurements made through these three analyses. We emphasize that, though the photometric analyses are independent for each catalog, the object centroids were all drawn from the FOCAS catalog and were not relocated in subsequent analyses (*i.e.*, we have preserved the link between an given object name and its position of the WFPC2 chevrons, within all three catalogs). The "Core" magnitudes are seen to systematically underestimate the fluxes of the brightest objects, as expected given that their angular sizes extend well beyond the 1.5″ diameter aperture. Note that the effect is most significant for objects brighter than 23rd magnitude, which were all placed in a single magnitude bin during our spectral target selection process, and does not vary significantly with $V-I$ color. When comparing the two independent estimates for total magnitude, we find that the dominant source of variation is the scatter in the measurements at faint (below 23rd) magnitudes.

There are a few ($N \sim 20$) objects with large offsets from catalog to catalog; these extreme differences, on the level of two to five magnitudes, are primarily caused, in order of frequency and importance, by (a) difficulties in measuring fluxes for objects on the extreme edges of chips (centered within the outer 7″, where the background measurement has been compromised by the sharp decline in pixel responsivity and differences in estimating background levels assume a critical role), (b) overlapping objects which are not deconvolved identically by each set of algorithms, and (c) stellar diffraction spikes. We examined all such outliers, and found only one which could not be explained by one of these three factors: 063_2764, an extremely diffuse, extended low surface brightness object.

The FOCAS and Core catalogs show the fewest such offsets, as shown in the first three panels of Figure 3. The

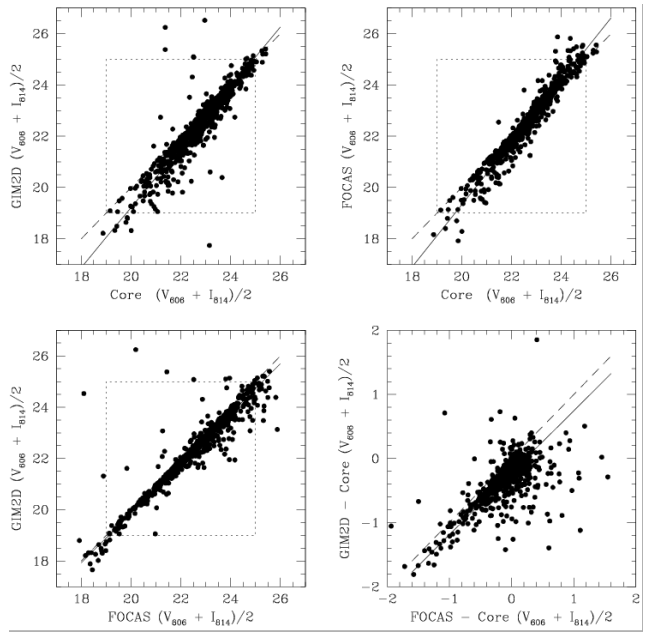

FIG. 3.— The dispersion of magnitudes throughout the three imaging analyses (FOCAS total, 1.5″ aperture Core, and GIM2D total) used for the GSS sample. The first three panels show the relative distribution of magnitudes between catalogs; the dashed line follows the relation $y = x$ and the solid line is an unweighted fit to objects between 19 and 25 magnitudes (boxed) differing by less than 2 magnitudes between catalogs. The final panel plots the difference between FOCAS and Core magnitudes versus the difference between GIM2D and Core magnitudes, with a fit to the same points as in the other panels. We find that the Core magnitudes systematically underestimate luminosity for the brightest objects, because their large angular diameters extend beyond the 1.5″ Core apertures, while the difference between FOCAS and GIM2D total magnitudes becomes more significant for objects fainter than 23rd magnitude. The final panel demonstrates that the offset for the Core aperture measurements is more significant than the scatter between the two estimates based on total magnitudes, as the data tend to be forcibly extended along the $y = x$ line by the Core offsets (with the brightest objects extending this trend preferentially to the lower left hand quadrant) rather than scattering uniformly about the origin.

GIM2D catalog is more sensitive to the first, and most common, cause of this type of error because its algorithms utilize a larger region around each object when determining the background flux level. It is thus likely that the GIM2D magnitudes are the least accurate measure of flux for an object when a substantial (greater than two magnitudes) difference exists between catalog entries.

When examining relative V_{606} and I_{814} magnitudes (*i.e.*, colors), we found that the independent centroiding between passbands in the FOCAS measurements produced a significant scatter in color overall, and an increase in colors at the extremes of the color distribution (particularly on the blue end). We describe two representative cases for clarity. In the first case FOCAS identified two objects separated by 0.9″ on the sky in I_{814}, one of magnitude 21.8 and the other 25.3. In V_{606}, a single object with magnitude 22.6 was placed within the same region. The single bright V_{606} detection was then matched to the fainter I_{814} object, while the brighter I_{814} object was assumed to have been undetected in V_{606}. The resultant mismatch produced an object with an artificially low I_{814} flux, resulting in an extremely blue color index. In the second case FOCAS split a "blobby" object into three separate objects on the V_{606} image, while melding the total flux into a single object on the I_{814} frame. The match of the total object in I_{814}

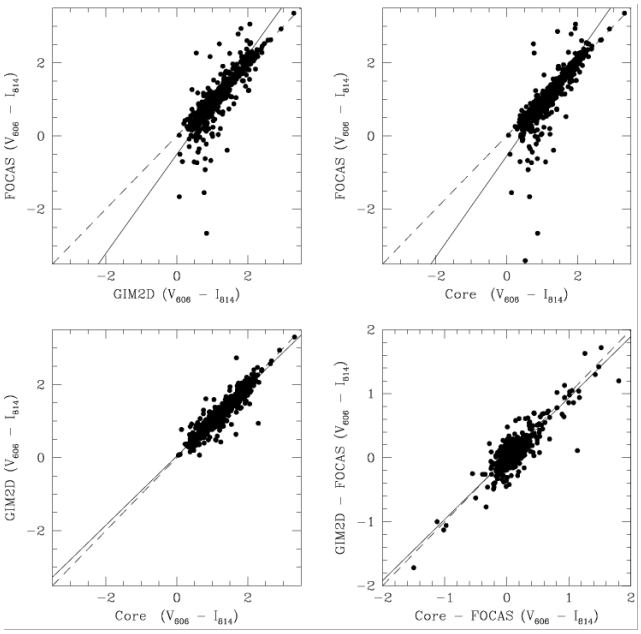

FIG. 4.— The distribution of colors throughout the three imaging analyses (FOCAS total, GIM2D total, and 1.0″ aperture Core) used for the GSS sample. The first three panels show the relative distribution of $V_{606}-I_{814}$ color between catalogs; the dashed line traces the relation $y = x$ and the solid line is an unweighted fit to objects between 19 and 25 magnitudes differing by less than 2 magnitudes between catalogs (no significant change appears in the fits if we relax these magnitude limits). The final panel plots the difference between GIM2D and FOCAS colors versus the difference between Core and FOCAS colors, with a fit to the same points as in the other panels. The FOCAS-derived colors contain some substantial outliers, particularly in a population of objects with extremely blue measurements of color which are not reproduced in the other two catalogs. The final panel demonstrates that this offset is more significant than the difference between the GIM2D and Core estimates of colors (which are offset by less than half a magnitude), as the data tend to be forcibly extended along the $y = x$ line by the FOCAS offsets rather than scattering uniformly about the origin.

versus a single component in V_{606} produced an extremely red color index. These outlying cases can be characterized by total object areas which differ greatly (by factors of 10 to 90) between the two frames (versus a factor of $\sim$ three across the rest of the data set). These objects are mainly found in the luminosity range between 23rd and 25th magnitudes. Extremely blue and extremely red objects were rated to be of considerable importance within our spectroscopic program, thus it was a priority to determine accurate colors for them.

The use of a single set of object positions for both the V_{606} and the I_{814} images in the Core and GIM2D catalogs provides a more robust estimation of the relative flux (though the background levels were still set independently within each passband). We note that the 1.0″ aperture Core colors are 0.03 ± 0.15 magnitudes redder than those determined for the entire galaxy with the GIM2D package, where the positive offset could be due to a slight nuclear concentration of redder stellar populations in many objects.

One of the science projects driving the spectral program was the modeling of photometric redshift estimates based on multi-color broad-band photometry (Brunner 1997; Brunner, Connolly, & Szalay 1999). We were actively searching for a small population of faint galaxy candidates with extremely blue colors, to use to improve the models, as well as trying to study the evolution of extremely blue and red objects. The color information used for sample selection was thus deemed to be quite important. For this reason, we elected to use aperture colors, and magnitudes, when creating the spectral sample.

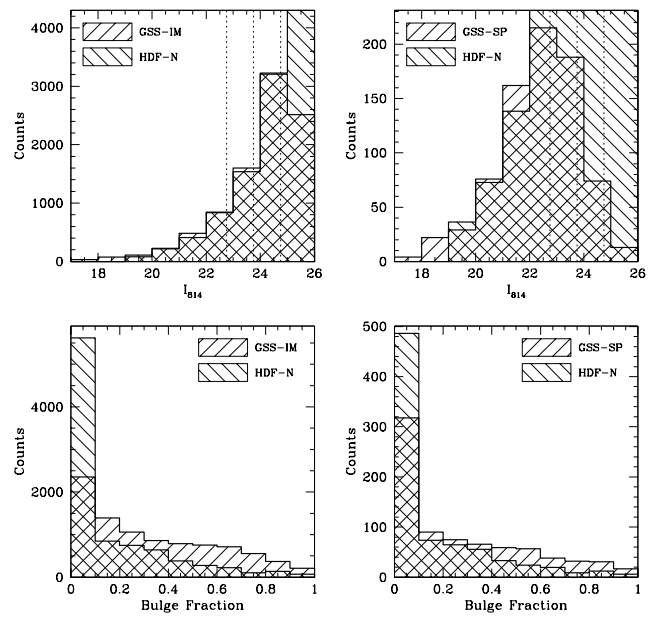

FIG. 5.— The distribution of number counts and bulge fractions as a function of $I_{814}AB$ magnitude. Dotted lines on the top panels show the three bins used in the spectroscopic target selection, with a fourth bin for fainter objects extending down to $I_{814}AB = 26$. The top left hand panel shows the distribution of number counts for the 9212 objects in the GSS imaging catalog and the 522 within the HDF-N field imaging catalog (Marleau & Simard 1998). The HDF-N catalog extends considerably deeper at faint magnitudes ($I_{814}AB > 25$) than the GSS catalog, due to the extremely deep, repeated exposures of the field. However, there is quite good agreement in the distribution within the limits of our spectral sample $(V_{606}+I_{814})/2 \leq 25$ (note that $(V_{606}+I_{814})/2$ in the Vega system is roughly equivalent to I_{814} in the AB system). The top right hand panel compares the number counts for the GSS spectral sample with the HDF-N field catalog. There is reasonable agreement in the distribution within the limits of the brightest bin of our spectral sample where $(V_{606} + I_{814})/2 \leq 23$. The bottom panels compare the bulge fraction distribution within the HDF-N imaging catalog and the GSS spectral sample, finding an excess of no bulge component objects in the HDF-N sample which is concentrated at faint magnitudes and does not hold for objects brighter than $I_{814}AB = 23$.

Figure 5 evaluates the depth of the HST+WFPC2 imaging, and the consequent limits to the photometric catalogs, by comparing two analyses of I_{814} data conducted with the GIM2D package. We compare the distribution of number counts (Marleau & Simard 1998) within the drizzled and deeply imaged HDF-N field (Williams et al.1996) with those within the GSS imaging catalog, scaling the absolute number of counts (522 versus 9212, for objects brighter than $I_{814} = 26$) by the relative surface areas (4.5 versus 127 square arcminutes), and find good agreement down to $I_{814} = 25$, with major differences becoming apparent beyond 25 magnitudes. Note that V_{606} data were not used in the GIM2D HDF-N analysis and are thus not available for comparison, and also that the HDF-N I-band magnitudes were cataloged under the AB system. A parallel comparison with the 785 objects in the GSS spectral sample with GIM2D parameters yields more scatter, but the agreement is still reasonable for objects brighter than $(V_{606}+I_{814})/2 \leq 23$.

The distribution of bulge fractions within the HDF-N sample contains an increase in objects best fit with no bulge com-

ponent, relative to both the GSS imaging and the GSS spectral samples. This effect is strongest for faint objects, and is not significant below 23 magnitudes. This is both because the difference in bulge fraction distributions is not present in the brighter objects, and because the number of objects has dropped to 72 for HDF-N sample, decreasing the statistical significance of the comparison process. Given the catalog limits, we speculate that these objects may be low surface brightness late-type spiral galaxies, falling below the surface brightness sensitivity of the GSS samples.

In summary, we estimate the 5σ detection limit of the imaging catalogs to lie at $(V_{606}+I_{814})/2 = 25$ (though note that surface brightness completion becomes an issue for significantly brighter objects, at roughly 23 magnitudes). Note that errors on individual magnitudes are 0.02 for observed quantities, and 0.02 – 0.03 for derived rest-frame magnitudes (see Simard et al. 2002 for complete details of such).

6. SAMPLE SELECTION

A series of spectroscopic samples was then selected, using the Core (1.5″ diameter aperture) magnitudes and the Core (1.0″ diameter aperture) colors to define the distribution of fluxes. Targets were selected to populate three magnitude bins, and divided into five color bins as well, for a general redshift survey. Table 2 shows the distribution of the completeness ratio (fraction of objects from the imaging catalog within each bin targeted for spectroscopy) for the total spectral survey program, which includes a set of objects chosen for additional properties (described in detail below) as well as the general redshift survey.

The primary magnitude limit for the general survey was $(V_{606}+I_{814})/2 = 24$, well above the detection limit of 25 for photometric completeness (though see Simard et al. 1999 for a discussion of the effect of surface brightness biases). This limit was chosen to lie well above the completeness level of the optical catalogs, as established by comparison with the data for the deeply imaged HDF-N field (see Figure 5), and to obtain sufficient spectral flux for redshift determination of objects exhibiting a range of morphologies (*e.g.*, both absorption and emission dominated spectra).

There are 83 objects with magnitudes between 24 and 25 for which spectra were obtained, for the following reasons. The pool of viable targets was deliberately widened to 25 magnitudes when sampling chevron 7, to extend the spectral survey to fainter magnitudes in the region where our photometry was significantly deeper than the norm. This resulted in observations of 28 objects which lay below the primary magnitude limit. Six additional faint objects were included as they were high priority targets for special subsamples (R#, hi-z, or phz, defined in Table 3). Twelve more "filler" objects were included due to a lack of brighter previously undetected spectral candidates within a given "slit position" along the GSS, serving as candidates of last resort for the north-eastern end of the GSS where our spectral observations were most concentrated. Finally, 37 objects with magnitudes between 24 and 25 were obtained serendipitously, falling within slits designed for brighter targets. There are also six fainter *serendipitous* objects within the spectral sample, lying between 25th and 25.5^{th} magnitude.

Note that Table 2 contains data on 788 objects from the spectroscopic sample, omitting 30 objects for which Core magnitudes could not be measured due to object close proximity to a WFPC2 chip edge or interfering stellar diffraction spikes. In addition, five stars selected for use in the mask alignment process are contained within this sample that were not listed in the spectroscopic sample described in Weiner et al. 2005a.

Figure 6 shows the distribution of the imaging and the spectral samples in color and in magnitude. We prioritized objects with blue colors ($V_{606}-I_{814} < 0.5$) or with red colors ($V_{606}-I_{814} > 1.75$) in the selection process; they are thus overrepresented in the spectral sample at a higher fraction (150%) than objects with intermediate colors in the range above 24th magnitude. Because the five color bins were chosen to be symmetric about the total color distribution, however, this did not significantly affect the relationship of average color as a function of magnitude in the spectral subsample. In both samples, average V_{606} - I_{814} colors are relatively constant for magnitudes brighter than 23 and then begin to shift blueward, at a rate of 0.2 magnitudes in color per unit of total magnitude.

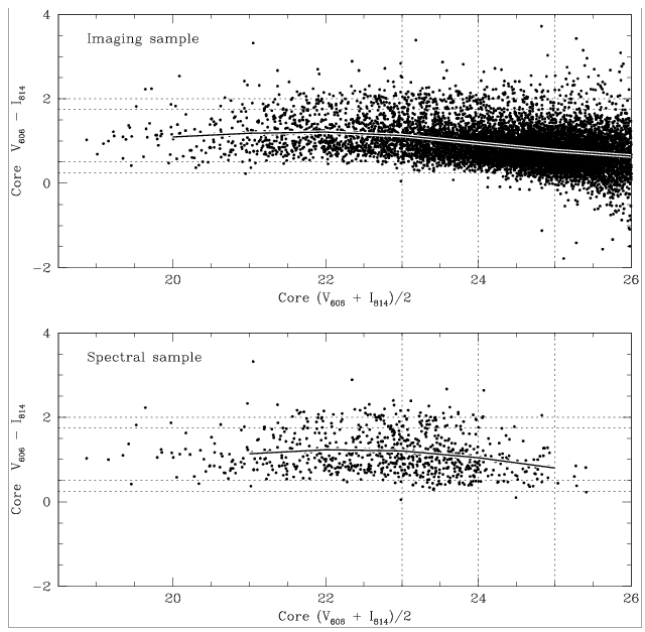

FIG. 6.— The distribution of Core color (1.0″ diameter aperture) versus Core magnitude (1.5″ diameter aperture) for the magnitudes used in spectral target selection, for (a) the complete imaging catalog and (b) the spectral subsample selected to observe with Keck+LRIS. Colors have been averaged in half-magnitude running bins, and the average values are connected with a line against the field of objects to show the mean trend. The dotted lines divide the space into fifteen blocks brighter than $(I_{814}+V_{606})/2 = 25$; each bin was tracked separately through the spectral target selection process.

7. SPECIAL SUBSAMPLES

One could say that the spectroscopic program was designed in an umbrella factory, in the sense that a host of scientific subprograms motivated the inclusion of various subsamples of objects, chosen with additional criteria beyond the described optical magnitudes and colors. In addition to the general magnitude limited sample defined above, several types of objects were prioritized in small numbers for selection from the photometric catalog. Table 3 gives a brief description of these additional selection criteria and their fractional representation within the complete spectral sample. We emphasize that almost all of these objects were also eligible for selection as a part of the general redshift survey (the exception being six serendipitously observed extremely faint objects which fall beyond the magnitude limit).

TABLE 2
OBSERVED SAMPLE COMPLETENESS

Color		$m = (V+I)/2$			
		$m \leq 23$	$23 < m \leq 24$	$24 < m \leq 25^a$	$25 < m \leq 25.5^b$
$V-I \leq 0.25$	(bluest)	1/2	0/2	1/99	1/194
$0.25 < V-I \leq 0.50$	(blue)	6/16	29/90	10/454	2/387
$0.50 < V-I \leq 1.75$		333/941	229/1354	60/2613	3/1372
$1.75 < V-I \leq 2.00$	(red)	36/85	27/72	2/52	0/19
$2.00 < V-I$	(reddest)	30/61	15/55	3/56	0/28

[a] The bulk of the objects within one magnitude below the spectroscopic survey limit are split between *serendipitously* observed objects, which fell within slits designed for brighter targets, and objects drawn from the single deeply imaged WFPC chevron number 7.
[b] All six objects fainter than 25th magnitude are *serendipitous* detections.

TABLE 3
SELECTION CRITERIA KEYS

Key	Description	#	%
zsurvey	redshift sample	566	69.2
serendip	companions (on shared slitlet)	121	14.8
disk	elongated galaxies, I < 22.5	64	7.8
align	mask alignment pointers (mostly stars)	27	3.3
phz	photometric redshift calibrators	12	1.5
R#	optical counterparts to known radio source	9	1.1
morph	morphologically selected	7	0.9
group A, B	members of 2 small groups on the sky	6	0.7
hi-z	dropout candidates	5	0.6
cfrs	CFRS targets with no redshifts	1	0.1
total	all spectral targets	818	100.0

The bulk of the spectral targets were selected for the general redshift survey program (keyword *zsurvey*). In addition to these primary targets, which were each placed within an individual slitlet, we acquired spectra for a set of secondary objects (*serendip*), which also fell within the same slitlets. Thus, multiple objects were on occasion observed within a single slitlet. This usually occurred by chance, though occasionally by design, where two objects fell together within a single default slit length, along or near to the default mask angle (40.5°). Some of the serendipitously detected objects are extremely faint, and thus we would never have selected them as primary candidates for spectroscopic follow-up due to the difficulty in getting enough spectral flux into the slitlet. These objects (characterized by faint broad band magnitudes and very low spectral continuum levels) were typically detected through the fortuitous discovery of an extremely bright, isolated emission line.

A third set of objects (*disk*) were chosen to allow the acquisition of spatially resolved velocity profiles (Vogt et al. 1996, 1997, 2005). In spite of the misleading keyword, these objects were not selected for a disklike morphology. They were chosen instead for angular elongation on the sky, equivalent to an inclination angle greater than 30° for a late-type spiral disk, and for a position angle such that the major axis lay within 30° of the Keck+LRIS mask angle (held at 40.5°). These simple criteria allowed the selection of early type galaxies, for example (*i.e.*, for which a spatially extended spectrum, composed purely of continuum and absorption features but with no emission was typically observed). Because of the need for high S/N spectra, these objects were prioritized only at the bright end of the luminosity distribution ($I_{814} \leq 22.5$).

Every Keck+LRIS mask which was constructed (see description below) contained a set of slitlets for science objects, and then because the targets were uniformly faint a small number of additional boxes (from three to six square slitlets) were added for bright, pointlike objects (*align*) used in the mask alignment process. All but two of these objects were stars (plus one QSO and one compact galaxy), and as these alignment objects were observed along with the science targets we have spectra for them (albeit at lower resolution, as the boxes are two arcseconds wide).

As mentioned earlier, we prioritized a set of faint, extremely blue targets (*phz*) because we lacked spectra to match HST-resolution images of such targets in sufficient numbers to calibrate photometric redshift models.

The remaining four subsamples each contain less than 10 members. For the first set of spectroscopy observations of the leftmost one-third of the strip (see Figure 2), we overlaid the detections found in the field at radio wavelengths within chevrons 6 or 8-10 (Fomalont et al. 1991) and placed slitlets upon those for which an optical counterpart brighter than 24th magnitude existed (*R#*). An additional set of candidates was chosen, particularly in the deeply imaged chevron 7, by eye for morphological peculiarities (*morph*). They each have either a diffuse light distribution, or appear to be a potential merger in progress, or are a gravitational lens candidate (one object). Six objects well within the magnitude limits of the redshift sample were included because they appeared to make up two small groups in projection on the sky (*group A, B*). A final two objects were included because they fell within the region of the strip which had been observed as a part of the CFRS (*cfrs*) redshift survey (Lilly et al. 1995), and redshifts had not been determined from the CFHT spectra.

Combining all objects placed within slitlets and the objects placed within square boxes for alignment purposes, spectra were obtained for a total of 818 unique objects.

Due to the additional selection criteria, the total set of spectroscopic targets is not a strictly random subsample of the photometric catalog as defined by our magnitude limits. In practice, however, the observed objects sample the range of apparent color and magnitude in the photometric catalog

fairly evenly in the range $(V_{606}+I_{814})/2 \leq 24$, as shown in Figures 7 through 11 for key structural parameters. Note that Simard et al. 2002 and C. N. A. Willmer et al. (2005, in preparation) also discuss the detailed selection map in apparent color-magnitude bins.

8. MODELING SAMPLE SELECTION

A set of Monte Carlo simulations was run, selecting objects from the imaging catalog purely by aperture magnitudes and colors in the fifteen bins to match the fractions listed in Table 2. We began by trimming the spectroscopic sample from 818 to 782 objects. We first removed six faint, serendipitously observed objects which were fainter than the sample limit of 25 magnitudes. We then removed 30 objects for which Core magnitudes could not be measured, due to close proximity to WFPC2 chip edges or interfering stellar diffraction spikes. The imaging catalog was cut in a similar fashion to 6041 objects with both magnitudes brighter than 25 and a valid entry in the GIM2D catalog. (Note that 947 objects brighter than 25 were fit by FOCAS but not by GIM2D, which requires a larger background area around the object on the sky.)

Each "mock spectroscopic catalog" contains 782 objects, distributed identically to the spectroscopic sample within the five color bands and three magnitude bands used in sample creation. Figure 7 shows the distribution of magnitudes and colors for the spectroscopic sample and ten mock samples, finding reasonable agreement given the scatter in the mock catalog distributions. The number of objects within each broad magnitude bin is identical for the Core magnitudes and colors, by design.

We observe that the spectroscopic sample contains a slight excess of the brightest objects within the 23rd magnitude band (and thus a dearth of the faintest objects), due in part to the preferential inclusion of bright stars used in the mask alignment process. Within the 24th and 25th magnitude bands, we again see a slight bias towards including brighter objects at the expense of fainter ones (*i.e.,* more objects between 23 and 23.5, or 24 and 24.5, than expected, coupled to less objects between 23.5 and 24, or 24.5 and 25). This effect is not larger than the variance in magnitudes as measured by different techniques, and becomes washed out in the right hand panel for magnitudes derived with the GIM2D package.

Figure 8 shows the distribution of half light radii, bulge fractions, R_A asymmetry indices (also defined as *ra*3; *cf.,* Schade et al. 1995; Simard et al. 2002), a measure of the residual flux remaining for each object after subtracting a doppelganger formed by rotating the object image through 180° on the sky, and position angle on the sky for the spectroscopic sample and ten mock samples. There is a slight trend towards including larger objects (by angular size) in the spectroscopic survey. The one solid difference between the spectroscopic sample and the mock samples, however, is found when examining the distribution of position angles on the sky. This distribution should be relatively flat, though the variance in the mock sample distribution indicates the level of scatter. As expected, we observe an excess of objects within the spectral sample at low position angles. The cause for this trend is the prioritized selection of elongated objects (*disk* classification) for which the position angles lie within 30° of the angle on the sky at which the Keck+LRIS masks were placed, causing an excess of objects within 10° and 70°. There is a 12% increase across this range, a 4σ variation given the scatter in the mock catalog distributions.

Note that this selection effect affects the position angle dis-

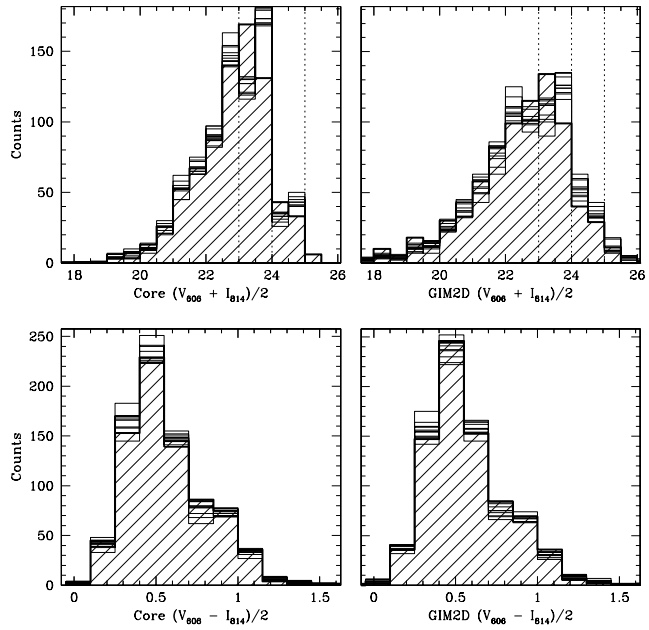

FIG. 7.— The distribution of Core and GIM2D magnitudes and colors, for the spectroscopic sample (the hatched histogram, outlined with a heavy line) and ten simulated samples drawn from the imaging catalog with the magnitude and color selection criteria for the spectroscopic survey but using no additional criteria (*e.g.,* morphology). There is reasonable agreement between the simulated and the actual samples, though a slight trend exists towards brighter objects within each broad magnitude bin for the spectroscopic sample Core magnitudes (caused in part, in the brightest magnitude bin, by the inclusion of bright stars used as mask alignment objects.

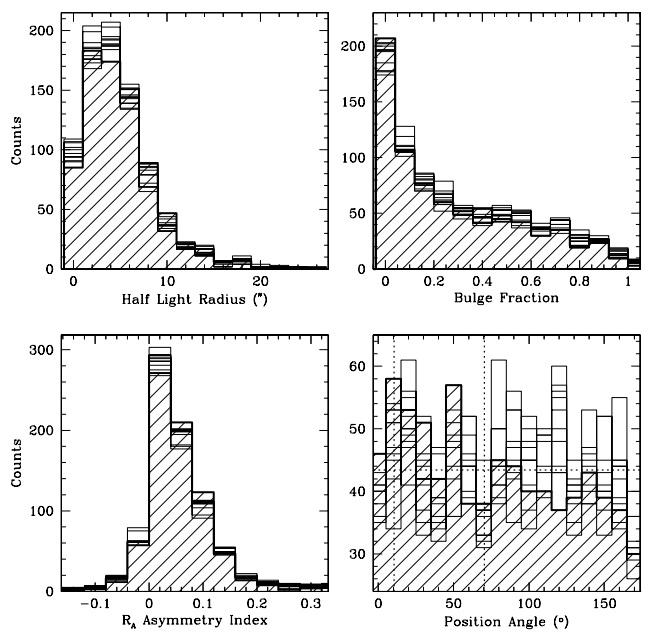

FIG. 8.— The distribution of angular half-light radii, bulge fractions, R_A asymmetry indices, and position angles on the sky, for the spectroscopic sample (the hatched histogram, outlined with a heavy line) and ten simulated samples drawn from the imaging catalog with the magnitude and color selection criteria for the spectroscopic survey but using no additional criteria (*e.g.,* morphology). There is reasonable agreement between the simulated and the actual samples for the first three panels. The 4σ bias in position angle towards low values (the dotted horizontal line represents a perfectly even distribution) is caused by the preferential selection of elongated objects for which the position angle of the major axis lay within 30° of the Keck+LRIS mask angle of 40.5° (the region marked by dotted vertical lines) within the spectroscopic sample.

tribution but does not translate into a significantly larger than expected fraction of, for example, objects with small bulge fractions, as shown in the top panel. Accounting for the 27 mask alignment objects (*e.g.*, excess stars, which tend to be fit with a bulge profile of zero) within the spectral sample, no significant differences remain in bulge distributions. In summary, the selection of a small subset of objects based on additional factors (*e.g.*, apparent morphology) in the actual spectral sample does not appear to have significantly affected the distribution of structural parameters other than position angle on the sky.

We examine the distribution of objects within the complete imaging catalog in Figure 9, plotting half light radii, bulge fractions, and R_A asymmetry indices against magnitude. In order to characterize the distributions, the data were binned into a 20×20 grid within each panel. Contours were then fit to each grid image, running from 5% to 75% of the peak values.

Figure 10 contains the subset of data forming the spectral sample, plotted in similar fashion. However, the contours in Figure 10 are not fit to the spectral sample. Instead, the grid images for the total imaging catalog from Figure 9 were convolved with a spectral luminosity selection function, and used to form a set of contours which reflected the magnitude selection of the spectral sample. This selection function was formed by sampling the ratio of counts within the spectral sample to counts within the parent imaging catalog, for each of the 20 bins formed by the columns of the contour image grid (analogous to dividing the counts in the first panel of Figure 10 by those in the first panel of Figure 9). The effect is to multiply each grid point by the fraction of objects selected for spectroscopic follow-up within the associated luminosity bin.

The resultant contours match the distribution of the spectra sample quite well, and are in fact indistinguishable from contours drawn directly from the spectral sample data. Figure 11 shows this comparison explicitly, overlaying the two sets of contours against each other. The differences between the distributions within each panel are not statistically significant.

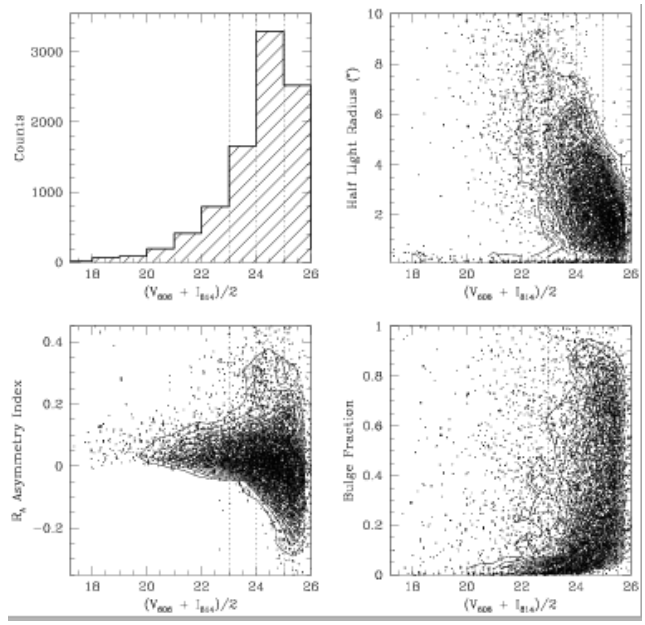

FIG. 9.— The distribution of (a) number counts, (b) half-light radii, (c) R_A asymmetry indices, and (d) bulge fractions as a function of magnitude for all objects within the imaging catalogs, as determined with the GIM2D structural analysis package. Dotted lines on every panel separate the points into the three bins used in the spectroscopic target selection, with a fourth bin for fainter objects extending down to $(V_{606} + I_{814})/2 = 26$. The twelve contours overlaid on the last three panels extend from 5% to 75% of peak values.

9. MASK DESIGN

The DEEP1 spectra were taken as part of a multi-year spring season spectroscopy program at the Keck Observatory, using the LRIS spectrograph (Oke et al. 1995). Observations of the GSS were conducted over nine observing runs on 25 nights within a five-year period, in conjunction with several other spring fields, and thus the process and technique for object selection was adapted with passing years as the technology of manipulating large field images matured (*e.g.*, memory allocation). A total of 36 slit masks was constructed for the strip, each containing between 30 and 55 objects.

An initial set of fifteen LRIS slit masks was constructed in 1995. We had no equipment which would allow us to create slitlets at an arbitrary mask angle at this time, so spectra were taken for all objects at the same position angle on the sky (40.5°) regardless of the angle of any spatial elongation of the object. Individual slitlets were 1″ in width and 12″ in length, and each mask contained roughly 30 of them. The bulk of the objects was selected for the general redshift survey, and a set of alignment objects was included on every mask.

The Groth Strip is roughly four arcminutes wide, and so we attempted to place objects from only the upper or the lower half within a single mask, so as to keep the shift in observed spectral range as small as possible from object to object. Once objects were selected for the spectral program, they were placed upon either one, two, or four masks, depending upon the faintness of the target. Objects brighter than 23 in $(V_{606} + I_{814})/2$ were placed initially on a single mask, those between 23rd and 24th magnitude were placed on two masks, and the faintest objects, below 24th magnitude (drawn primarily from the deeply imaged chevron 7), were placed on four masks to maximize the amount of spectral flux that we would obtain.

Throughout the spectroscopy program, each mask was observed in turn with a blue wavelength grating (typically 900 l mm^{-1}/5500Å) and a red wavelength grating (600 l mm^{-1}/7500Å), to create a combined spectrum covering the range 5000Å to 8200Å. We planned for 2×1500 seconds exposure per grating per mask.

From 1996 onward, the minimum acceptable slit-length was allowed to drop to 8″, as one could extract usable spectra reliably with background regions on each side of the object of smaller spatial extent due to the overall brightness of the continuum level and strong key emission and absorptions features. A small fraction of all slits were tilted at an angle (between 10.5° and 70.5° eastwards of north), in order to trace along the major axis of a spatially elongated object or to capture two objects within one slit. As a result of these changes, the average number of objects per mask rose to 45.

The effect of the distribution on masks along and across the entire Groth Strip can be observed in the lower panels of Figure 2. The large, broad peak at -20 arcminutes in the left hand panel reflects our initial focus in a region surrounding the deeply imaged chevron 7. Note that the spectral fraction, the fraction of the imaging catalog objects which were observed with Keck+LRIS, occasionally rises above a level of one, as all spectral targets were counted but the normalization

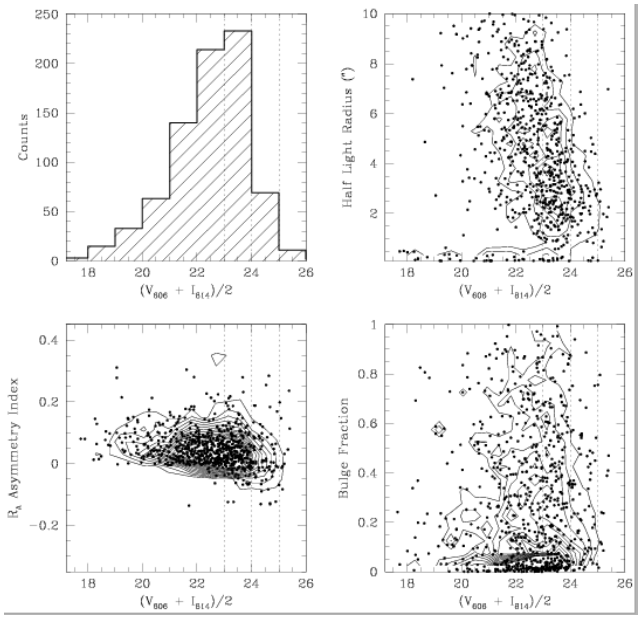

FIG. 10.— The distribution of (a) number counts, (b) half-light radii, (c) R_A asymmetry indices, and (d) bulge fractions as a function of magnitude for the spectroscopic sample. Dotted lines on every panel separate the points into the three bins used in the spectroscopic target selection, with a fourth bin for fainter objects extending down to $(V_{606} + I_{814})/2 = 26$. The spectral sample is biased toward the bright end of the magnitude selection bins; the fraction of imaging targets contained within the spectral sample drops off significantly below $V_{606} + I_{814} = 24$, in the two faintest bins (due to the increase in the number of possible targets and the decrease in targeting priority below this limit). Note that a comparison of bulge fraction histograms between the imaging and spectroscopic samples, showing good agreement, can be found by comparing the two lower panels in Figure 5. The twelve contours overlaid on the last three panels were created by convolving the distribution of the parent imaging sample, shown in Figure 9, with the fraction of objects selected as a pure function of luminosity – they are not fit to these data. Note the agreement between the distribution of the spectral sample and the contours, indicating that our complex selection function can be treated as one of magnitude without bias in these key parameters.

was to the limits of the general redshift survey ($(V_{606} + I_{814})/2 < 24$). The right hand panel shows a slight increase in spectral fraction along the top half of the chevrons (chips 2 and 3), caused by the distribution of masks along either the top of the bottom of the strip.

10. POSTAGE STAMPS

A catalog of annotated V_{606} and I_{814} images has been created for the entire spectral sample observed with Keck+LRIS (Figure 12 is a representative sample). Each image is overlaid with the position of the LRIS slitlet at which it was observed, and labeled with a set of spectral- and image-derived parameters. A single representative panel is shown here, and the entire set is available at the DEEP web site at `http://deep.ucolick.org`.

11. SUMMARY

This paper describes the framework and observational basis for first five-year phase (DEEP1) of the Deep Extragalactic Exploratory Probe (DEEP), a longterm, multifaceted study of the formation and evolution of galaxies in the distant Universe. We have obtained complete HST imaging in I_{814} and V_{606} of the Groth Survey Strip, a 127 square arcminute region in the northern hemisphere sky, and conducted Keck+LRIS spectroscopy of 818 objects in a redshift survey which extends down to magnitudes of $(V_{606}+I_{814})/2 = 25$.

Though our selection criteria for the spectroscopic subsample are complex, and have varied as the survey progressed, the bulk of the objects were selected to match the range in colors and magnitudes at the bright end (*i.e.*, $(V_{606}+I_{814})/2 \leq 25$) of the imaging catalog. We model the complete spectroscopic subsample, and show that it can be reproduced statistically by making straightforward cuts in magnitude and color in the parent imaging catalog. The sole exception to this statement lies in the distribution of position angles on the sky, where we observe an expected bias towards objects with major axes oriented along the position angle at which the Keck+LRIS masks were aligned.

The authors recognize and acknowledge the cultural role and reverence that the summit of Mauna Kea has always had within the indigenous Hawaiian community. We are most fortunate to have the opportunity to conduct observations from this mountain. The authors thank the staffs of HST and Keck for their help in acquiring these data, the W. M. Keck Foundation and NASA for construction of the Keck telescopes, and Bev Oke and Judy Cohen for their work on LRIS that enabled the spectroscopic observations described herein. We give our thanks to the anonymous referee of this manuscript, who showed a careful and courteous eye for detail. NPV is a Guest User, Canadian Astronomy Data Center, which is operated by the Dominion Astrophysical Observatory for the National Research Council of Canada's Herzberg Institute of Astrophysics.

This work was conducted under the auspices of the DEEP (Deep Extragalactic Evolutionary Probe) project, which was established through the Center for Particle Astrophysics. Funding was provided by NSF grants AST-9529098, AST-0071198, by AST-0349155 to NPV through the Career Awards program, and by NSF–0123690 via the ADVANCE-IT Program at NMSU, and by NASA grants GO-07883.01-96A, GO-10249.01A, and AR-05801.01-94A, AR-06402.01-95A, and AR-07532.01-96A. HST imaging of the Groth Strip was planned, executed, and analyzed by EJG and JR with support from NASA grants NAS5-1661 and NAG5-6279 from the WFPC1 IDT. SMF would like to thank the California Association for Research in Astronomy for a generous research grant.

APPENDIX

APPENDIX A: PARTICULARS OF DEEP1 GSS MASK DESIGN

The DEEP1 Groth Strip spectroscopic survey was a multi-year pilot program, designed to find the observational limits of the Keck+LRIS equipment and to explore a variety of scientific programs. For these reasons, as well as the rapid parallel advances in computer technologies, the object selection process evolved with time. We present here a detailed overview of the creation process for the entire set of 36 masks.

Sample selection for the first 15 masks was conducted by using a printed set of black and white I_{814} images of the target chevrons, mosaicked by hand into a single, extended map. Transparent overlays were coded to indicate object Core magnitudes

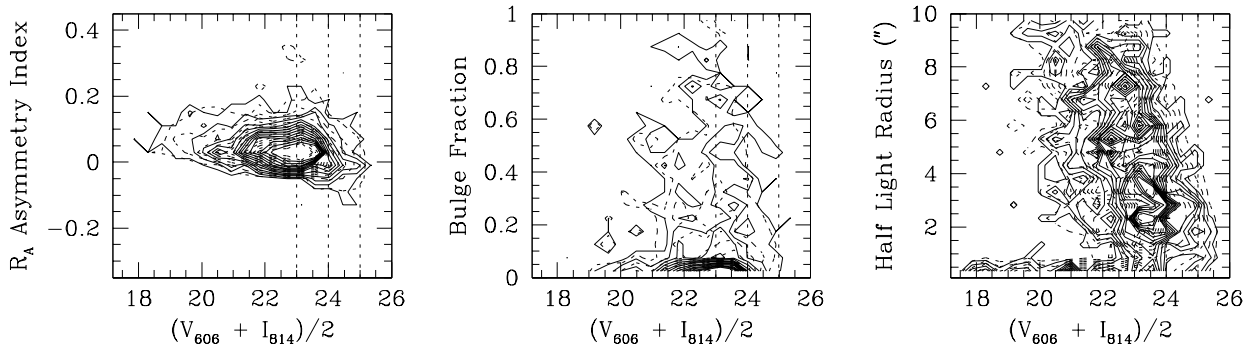

FIG. 11.— A set of contours fit to the distribution of the spectral sample (solid lines) are compared to those from Figure 10 (dotted lines), which were creating by convolving a set of contours fit to the distribution of the total imaging catalog with the fraction of objects observed in the spectral sample as a function of magnitude. In the first panel, note that the small dotted contour in the region of high R_A values falls at the lowest contour (5% of peak values), and is not statistically significant. Both distributions of bulge fractions (second panel) show a strong peak for objects with extremely low bulge fractions, while the distributions of half light radii (third panel) are broader. There is good agreement between the two fits in every panel.

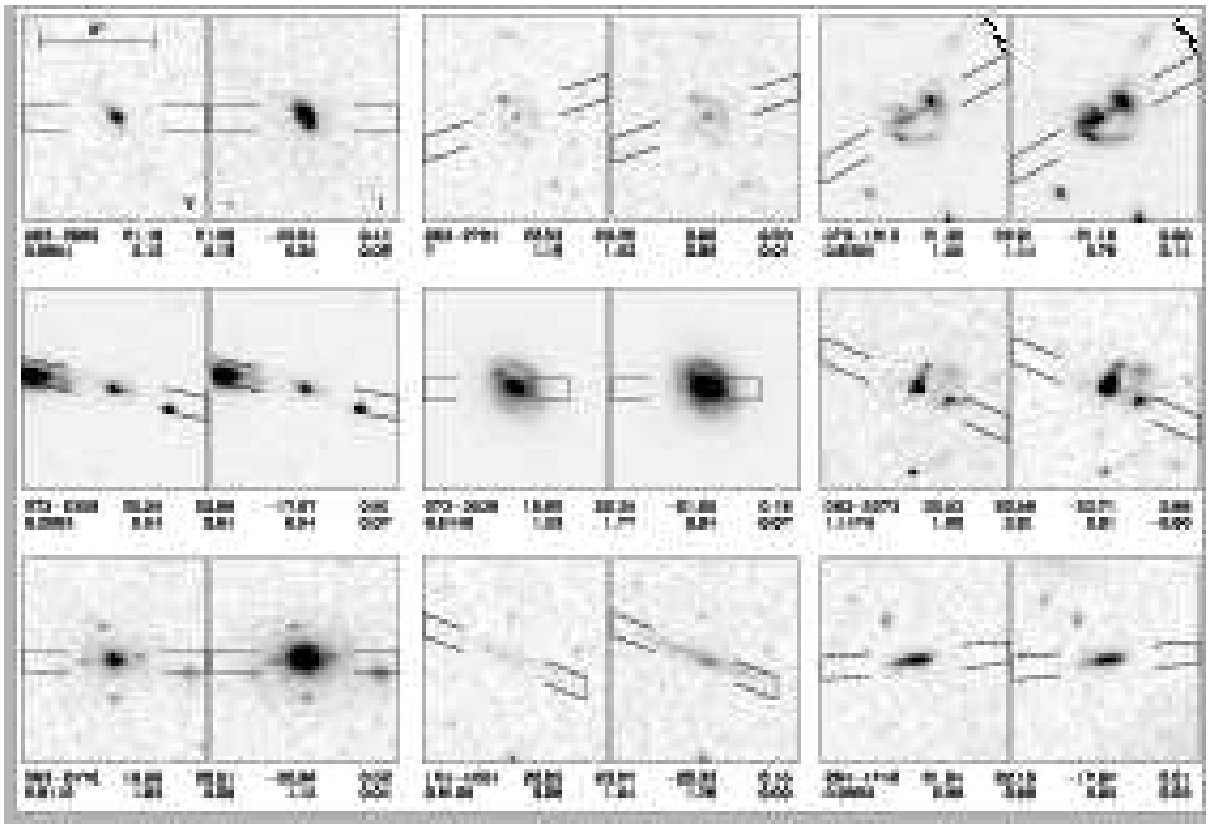

FIG. 12.— A representative set of V_{606} and I_{814} HST+WFPC2 images of objects within the spectral sample. The solid lines on each postage stamp image indicate the position of the KECK+LRIS slitlet upon the object. Each object is labeled by name, followed by total I_{814} GIM2D magnitude, aperture I_{814} Core magnitude, absolute B-band magnitude, and bulge fraction; the lower line contains redshift, $V_{606}-I_{814}$ GIM2D color, aperture $V_{606}-I_{814}$ Core color, half light radius in arcseconds, and asymmetry parameter R_A.

and colors. This first set of masks was placed to overlap with the deeply imaged chevron 7 at the northeast end of the strip (fourth chevron from the left end, in Figure 2), and extended from chevron 6 down to chevron 10. The first group of four masks (GSS1A, GSS1B, GSS1C, and GSS1D) had a single position on the sky and contained objects selected from chips 2 and 3 of the targeted chevrons, while the second and third sets of four (GSS2-ABCD, GSS3-ABCD) contained objects selected from chips 3 and 4 and were offset toward the lower edge of the Groth Strip. The final three masks (GSSB-abc) were back-up program masks designed for use in poor weather (low transparency conditions), with 1.2″ width slitlets. Each mask contained the brightest candidates from the GSS1, GSS2, and GSS3 series respectively, and were filled with additional bright objects in the range $(V_{606} + I_{814})/2 \leq 23$.

A few serendipitous spectra would be discovered during the spectral reduction process, and the entire set of *radio* and *group*

objects was selected at this time, as well as several *morphological* candidates. Note that no objects were selected according to the *disk*, *cfrs*, or *phz* key words for these early mask sequences (though the bluest and reddest objects were prioritized within the general redshift survey).

Beginning in 1996, masks were designed using interactive, computerized selection to select objects and to place them on the masks (NPV's `disktool` IRAF package). Following target and alignment star selection, all masks were modeled with ACP's `ucsclris` IRAF package to account for specific observational constraints (*e.g.*, anamorphic corrections) and to create machine (CAD) instructions for milling the mask locally in the UCSC instrumentation shops. The pattern of placing objects on one, two, or four masks according to brightness was maintained. In addition, any objects which were re-observed because of insufficient initial flux levels (*i.e.*, no redshift could be assigned) were placed on as many masks as were available, and objects with the reddest colors were automatically placed on at least two masks regardless of brightness (spectral reductions proved to be difficult for these objects, due to the presence of very little other than wide, diffuse absorption features). After the first year a small fraction of all slits were tilted at an angle ($\theta < 30°$) relative to 40.5°, in order to trace along the major axis of a spatially elongated object or to capture two objects within one slit. For the *disk* candidates, exposure time was doubled from one mask to two to increase S/N levels for rotation curve extraction.

In 1996, the thirteen unused masks were updated with several elongated *disk* candidates, several additional *morph* candidates, and a set of the *phz* objects with extremely blue colors. Because KPNO UBRI photometry had been obtained for the northeast portion of the strip in the intervening year, these data were used as well in the relative prioritization of the 17 *phz* candidates. The masks were updated in place, with original names retained. (Only masks GSS1-A and GSS1-B were used in 1995, due to bad weather.) In 1997 we created a new set of five masks (GSS4-ABCDE), shifting our default position along the top of the strip slightly to the right to include chevron 11. We ceased placing general targets on the masks which were fainter than (V_{606} + I_{814} = 24, as we found them to demonstrate unlikely success for redshift identification. Five UB dropout candidates (with photometric redshifts $z > 2.5$) were identified from the KPNO UBRI data and placed on four masks each. In 1998 seventeen additional masks were created (GSS5-ABC, GSS6-ABCDEF, and GSS7-ABCDEFGH). We began to employ tilted slits not only to trace the major axes of individual spatially extended objects but also to place secondary, and occasionally tertiary, *serendip* objects which were offset from primary targets by $\theta < 30°$ from the mask angle, to increase efficiency.

The GSS5 series was designed to re-observe objects from within chevrons 6 through 11 for which we still did not have redshifts, in spite of repeated observations. We prioritized objects in the following order: (1) previously observed targets with $I_{814} \leq 23$ and no secure redshift, (2) previously observed sources with $I_{814} \leq 24$ and no secure redshift, (3) previously observed sources with $I_{814} > 25$ and no secure redshift, (4) high redshift (U and B dropout) candidates determined from ground based UBRI data or from existing GSS spectra which showed promise (*i.e.*, no features indicating lower redshifts), and (5) CFRS survey objects without redshifts. The GSS6 series was placed at the southwest end of the strip. Two new pointings were established, and at each one two normal masks (ABDE) and one back-up mask (CF) with bright objects was created. The *disk*, *phz* and extremely red objects were prioritized in the sample selection process. The GSS7 series was placed in the middle region of the strip, designed to sample the bright end of the luminosity function and bridge the spatial gap between the northeast and southwest sampled portions. Four new pointings were created, and a normal mask (ACEG) and a back-up mask (BDFH) with bright objects were made for each one. The *disk*, *phz* and extremely red objects were again prioritized in the sample selection process; in addition as there would be only one mask exposure per position under optimum conditions, we limited the general redshift survey to $(V_{606} + I_{814})/2 \leq 23$.

In 1999 ten additional masks were created (GSS6-GHIJ and GSS7-IJKLMN). They were placed in sets of two at five of the six positions established in 1998 (the sixth pointing, home of masks GSS7-EF was not doubled because it had not been used in 1998).

We note two factors of interest to anyone studying interactions, pairs of objects, or large scale structure: (a) the repeated placement of fainter objects on a series of masks all centered at the same location, conducted to increase the total spectral flux and thus the probability of redshift determination for such objects, and (b) the requirement of a few (four to six) arcseconds of slit being available to each side of each object for background light removal. These both affect the object-to-object angular distribution within the spectral sample on small size scales ($\theta \sim 10''$). The first effect will further result in a sparser sampling of near neighbors on the sky for the fainter objects within the spectral sample.

APPENDIX B: CONVERSION FACTORS BETWEEN AB AND VEGA MAGNITUDES

The convolution between filter responses and galaxy SEDs followed Fukugita et al. (1995), by resampling filters and spectra to the same dispersion (1 Å), using parabolic and linear interpolations respectively. For the HST I_{814} and V_{606} filters, efficiency curves for WFPC2 were downloaded from the Space Telescope Science Institute web site and curves for the different CCDs were averaged. The Vega spectrum used to calculate the conversion to AB magnitudes is the model atmosphere calculated by Kurucz, distributed with the Bruzual & Charlot (2003) galaxy evolution synthesis package. The AB spectrum is simply a flat spectrum in $F(\nu)$ converted into wavelength space (*e.g.*, Fukugita et al. 1995).

TABLE B4
CONVERSION FACTORS BETWEEN AB AND VEGA MAGNITUDES

Transformation Between AB and Vega Systems		
$V606_{AB}$	=	$V606_{Vega} + 0.096$
$I814_{AB}$	=	$I814_{Vega} + 0.417$
$(V606-I814)_{AB}$	=	$(V606-I814)_{Vega} - 0.321$

REFERENCES

Abazajian, K., et al. 2003, AJ, 126, 2081
Arnouts, S., de Lapparent, V., Mathez, G., Mazure, A., Mellier, Y., Bertin, E., Kruszewski, A. 1997, A&AS 124, 163
Brunner, R. J. 1997, Ph.D. thesis, Johns Hopkins University
Brunner, R. J., Connolly, A. J., & Szalay, A. S. 1999, ApJ, 516, 563
Bruzual, G., & Charlot, S. 2003, MNRAS, 344, 1000
Casertano, S., et al. 2000, AJ, 120, 2747
Colless, M., Ellis, R. S., Taylor, K., & Hook, R. N. 1990, MNRAS, 244, 408
Colless, M., et al. 2001, MNRAS, 328, 1039
Conselice, C., Bundy, K., Ellis, R. S. E., Brinchmann, J., Vogt, N. P., & Phillips, A. C. 2005, ApJ, submitted
Cowie, L. L., Songaila, A., Hu, E. M., & Cohen, J. G. 1996, AJ, 112, 839
Cristóbal-Hornillos, D., Balcells, M., Prieto, M., Guzmán, R., Gallego, J., Cardiel, N., Serrano, Á., & Pelló, R. 2003, ApJ, 595, 71
Cohen, J. G., Hogg, D. W., Blandford, R., Cowie, L. L., Hu, E., Songaila, A., Shopbell, P., & Richberg, K. 2000, ApJ, 538, 29
Ellis, R. S. E. 1997, ARA&A, 35, 389
Fomalont, E. B., Windhorst, R. A., Kristian, J. A., & Kellerman, K. I. 1991, AJ, 102, 1258
Fukugita, M., Shimasaku, K., & Ichikawa, T. 1995, PASP, 107, 945
Gebhardt, K., et al. 2003, ApJ, 597, 239
Giavalisco, M., et al. 2004, ApJ, 600, L93
Hammer, F., Crampton. D., Le Fèvre, O., Lilly, S. J. 1995, ApJ, 455, 88
Holtzman, J. A., et al. 1995, PASP, 107, 156
Im, M. et al. 2002, ApJ, 571, 136
Im, M., Faber, S. M., Gebhardt, K., Koo, D. C., Phillips, A. C., Schiavon, R. P., Simard, L., & Willmer, C. N. A. 2001, AJ, 122, 750
Jarvis, J. F., Tyson, J. A. 1981, AJ, 86, 476
Kobulnicky, H. A. et al. 2003, ApJ, 599, 1006
Koo, D. C. et al. 1996, ApJ, 469, 535
Koo, D. C. 2000, Reviews of Modern Astronomy, 13, 173
Koo, D. C., et al. 2005, ApJ, 157, XXXX
Koo, D. C., & Kron, R. G. 1992, ARA&A, 30, 613
Le Fèvre, O., Crampton. D., Lilly, S. J., Hammer, F., & Tresse, L. 1995, ApJ, 455, 60
Le Fèvre, O. et al. 2004, A&A, 428, 1043
Le Fèvre, O., Crampton, D., Hammer, F., Lilly, S. J., & Tresse, L. 1994, ApJ, 423, L89
Lilly, S. J., Hammer, F., Le Fèvre, O., & Crampton. D. 1995, ApJ, 455, 75
Lilly, S. J., Le Fèvre, O., Crampton, David, Hammer, F., & Tresse, L. 1995, ApJ, 455, 50
Marleau, F., & Simard, L. 1998, ApJ, 507, 585
Oke, J. B., et al. 1995, PASP, 107, 375
Rhodes, J., Refregier, A., & Groth, E. J. 2000, ApJ, 536, 79
Schade, D., Lilly, S. J., Crampton, D., Hammer, F., Le Fèvre, O., & Tresse, L. 1995, ApJ, 451, 1
Simard, L., et al. 1999, ApJ, 519, 563
Simard, L., et al. 2002, ApJS, 142, 1
Vogt, N. P., Phillips, A. C., Faber, S. M., Gallego, J., Gronwall, C., Guzman, R., Illingworth, G. D., Koo, D. C., & Lowenthal, J. D. 1997, ApJ, 479, L121
Vogt, N. P., Forbes, D. A., Phillips, A. C., Gronwall, C., Faber, S. M., Illingworth, G. D., & Koo, D. C. 1996, ApJ, 465, L15
Weiner, B. J.et al. 2005a, ApJ, in press
Williams, R. E., et al. 1996, AJ, 112, 1335
Yee, H. K. C., et al. 1996, ApJS, 102, 289
Yee, H. K. C., et al. 2000, ApJS, 129, 475